

2012

Droplet Retention on an Incline

S. R. Annapragada
Purdue University

J. Y. Murthy
Purdue University

S V. Garimella
Purdue University, sureshg@purdue.edu

Follow this and additional works at: <http://docs.lib.purdue.edu/coolingpubs>

Annapragada, S. R.; Murthy, J. Y.; and Garimella, S V, "Droplet Retention on an Incline" (2012). *CTRC Research Publications*. Paper 160.

<http://dx.doi.org/doi:10.1016/j.ijheatmasstransfer.2011.09.057>

This document has been made available through Purdue e-Pubs, a service of the Purdue University Libraries. Please contact epubs@purdue.edu for additional information.

Droplet Retention on an Incline

S. Ravi Annapragada, Jayathi Y. Murthy and Suresh V. Garimella
Cooling Technologies Research Center, and NSF IUCRC
School of Mechanical Engineering and Birck Nanotechnology Center
Purdue University
West Lafayette, Indiana 47907-2088 USA
{asravi, jmurthy, sureshg}@purdue.edu

Corresponding Author: Suresh V. Garimella, Tel: +1 765 494 5621

ABSTRACT

The present study seeks to understand and predict droplet retention on smooth hydrophobic surfaces. The droplet shape and the advancing and receding contact angles are experimentally measured as a function of droplet size under the action of a gravitational force at different inclination angles. The advancing and receding contact angles are correlated with static contact angle and Bond number. A Volume of Fluid - Continuous Surface Force model with varying contact angles along the triple contact line is developed to predict droplet shape. The model is first verified against a twodimensional analytical solution. It is then used to simulate the shape of a sessile droplet on an incline at various angles of inclination and to determine the critical angle of inclination as a function of droplet size. Good agreement is found between experimental measurements and predictions. The contact line profile and contact area are also predicted. The contact area predictions based on a spherical-cap assumption are compared to the numerical predictions and are found to underpredict the droplet contact area.

1. INTRODUCTION

Droplets are widely encountered in various cooling applications, such as mist cooling [1,2], spray cooling [3,4], and even in traditional air conditioning and refrigeration applications involving dropwise condensation [5]. Emerging cooling techniques based on electrowetting propose to use droplet motion to transport heat [6-8]. Although many analytical, experimental and numerical studies [9] have explored droplet motion, the mechanics of the droplet while it is still in its static state, and just before motion starts, are not well understood. A study of static droplets would shed light on the threshold voltage [10] (or critical inclination) for initiating electrically (or gravitationally) induced droplet motion.

Before an actuated droplet begins to move, the droplet shape changes such that the forces acting at the triple contact line balance the actuation forces. These contact line forces are governed by the contact angles along the contact line. Macdougall and Ockrent [11] performed simple stage-tilting experiments and showed that contact line forces could be described in terms of contact angles and surface tension. Frenkel [12] arrived at a similar formula for contact line forces using energy methods. Later experimental studies have proposed various correction factors to these formulae [13-17]. A more basic approach to finding the retention force was adopted by ElSherbini and Jacobi [18-20] who studied sessile droplets on a slope both experimentally and theoretically. The contact line force was calculated based on an experimentally measured azimuthal contact angle variation around the droplet available in the literature [17]. A third-order polynomial curve fit was shown to describe the azimuthal variation of contact angle. The vertical cross-sectional profile of the drop was predicted by the two-circle method sharing a common tangent at the top of the droplet, while the triple contact line was approximated by an ellipse. The volume of the droplet was calculated by integrating the droplet profile around the circumference of the base [18]. In follow-up papers [19,20], this droplet profile model was used to predict the condensate retained on plain-fin heat exchangers. The maximum diameter of the droplets was predicted based on the force balance between gravity and contact line forces. The total retained condensate mass per unit area was predicted with advancing contact angle and angle of inclination as inputs.

Energy-minimization techniques have been widely used to model the static droplet shape on an incline [12,21-25]. Two-dimensional droplets were initially modeled using energy-based methods by Frenkel [12] and later by Merte and co-workers [21,22]. Frenkel provided upper bounds on the critical inclination for droplet sliding, whereas Merte and co-workers obtained 2D droplet shapes and receding contact angles with the advancing angle and critical droplet size provided as inputs. This analysis was extended to realistic, three-dimensional droplets by other researchers [23-25]. Iliev [25] obtained similar results with an equilibrium variational approach for three-dimensional droplets. The azimuthal variation of the contact angle was not provided. Milinazzo and Shinbrot [23] obtained the contact angle variation along the triple contact line as a function of Bond number, with the contact line assumed to be circular. They predicted a continuous azimuthal variation of the contact angle. Dimitrakopoulos and Higdon [24] numerically studied the critical condition for droplet stability and motion. The equilibrium shape was obtained from an optimization exercise. Additionally, the azimuthal variation of the contact angle along the triple contact line was also obtained from the simulations. The variation obtained was a step function from the advancing angle to the receding angle, with the transition occurring linearly between azimuthal angles of 45° to 90° . In spite of significant advances in energy-based techniques, internal fluid motion cannot be included in the model, and hence such techniques cannot provide insight into the physics of the droplet motion as it just starts to move.

Manna *et al.* [26] used stochastic simulations to model the shape of a 2D droplet on a vertical wall. The critical droplet size for sliding off the wall was captured, but the model was not extended to realistic 3D droplets. Brown *et al.* [27] used a finite element approach to model the 3D shapes of droplets on a slope as a function of the volume and angle of inclination. The contact angles around the droplet were obtained from the simulation. The drop was assumed to be pinned to the solid surface with a circular contact line. In reality, the droplet shape is not always circular, but instead, changes with the angle of inclination of the surface. Hence the assumption of a circular contact line is unrealistic.

Accurate force models need to be developed for static droplets, and the correct azimuthal variation of the contact angle along the contact line of the drop must be obtained. This requires a full three-dimensional simulation of the droplet, for which a Volume of Fluid (VOF) model combined with a Continuous Surface Force (CSF) representation of surface tension, is a suitable approach. The VOF model has been previously used in related problems, such as in the prediction of droplet splashing [28-31], transport through channels and columns [32-35] and recently, droplet motion [36]. It has been shown that a VOF approach in combination with static contact angle (SCA) models does not accurately predict the interface motion [29,32]. Hence various dynamic contact angle (DCA) models have been implemented. vanMourik *et al.* [33] compared the predictions of the interface motion in a tube under a changing gravitational force using various contact angle models in the VOF framework and found that Blake's theoretical model [37] predicted the experiments best followed by that of Seebergh and Berg [38].

In the present work, we address the prediction of the critical angle of inclination at which a droplet on an inclined plane begins to slide. A schematic diagram of the droplet and the associated terminology is provided in

Figure 1. We employ the VOF-CSF model, with the contact angle variation along the contact line being specified as an input. The model employs advancing and receding contact angles obtained from experiments conducted for the purpose as part of this work. The VOF simulation is then used to predict the critical angle of inclination at which sliding commences. Predictions of the critical angle of inclination so obtained are validated against our experimental measurements.

2. NUMERICAL MODEL

In the current work the VOF-CSF model in FLUENT [39] is used. A custom contact-angle model is implemented using user defined functions to capture the azimuthal contact angle variation.

2.1. VOF-CSF Method

In the VOF method, the flow of non-interpenetrating fluids is simulated by solving a single set of Navier-Stokes equations and tracking the volume fraction (α) of one or more secondary fluids in the entire domain. The volume fraction of the secondary phase (s) is obtained by solving the continuity equation for this phase:

$$\frac{\partial}{\partial t}(\alpha_s) + \nabla \cdot (\alpha_s \vec{v}_s) = 0 \quad (1)$$

The volume fraction of the primary phase (p) is calculated from:

$$\alpha_p + \sum \alpha_s = 1 \quad (2)$$

The shape of the interface is necessary to accurately calculate the advective and diffusive terms of the continuity equation in the finite volume formulation. For this purpose, Young's Geometric Reconstruction Scheme [40], which is based on piecewise-linear reconstruction of the interface in a partially-filled cell, is used. Further details of the implementation may be found in the FLUENT manual [39].

The momentum equation is solved for the average velocity of the mixture, and the influence of multiple phases appears through the phase fraction-dependent local properties of the material in each cell.

$$\frac{\partial}{\partial t}(\rho \vec{v}) + \nabla \cdot (\rho \vec{v} \vec{v}) = -\nabla p + \nabla \left[\mu (\nabla \vec{v} + \nabla \vec{v}^T) \right] + \rho \vec{g} + \vec{F} \quad (3)$$

where ρ is the density of the fluid, μ is the viscosity of the fluid. Here, the gravitational acceleration is specified as $\vec{g} = g \cos \beta \hat{i} + g \sin \beta \hat{j}$, as shown in Figure 1. Physical properties such as density and viscosity are volume-averaged as follows:

$$\rho = \alpha_s \rho_s + (1 - \alpha_s) \rho_p \quad (4)$$

$$\mu = \alpha_s \mu_s + (1 - \alpha_s) \mu_p \quad (5)$$

where subscripts p and s represent the primary and secondary phases, respectively. When only two phases exist, the volumetric force \vec{F} in Eq.(3) is given in the CSF formulation by:

$$\vec{F} = \sigma \frac{\rho \kappa_s \nabla \alpha_s}{\frac{1}{2}(\rho_p + \rho_s)} \quad (6)$$

Here σ is the surface tension coefficient between primary and secondary phases, κ_s is the interface curvature for the secondary phase given by Brackbill *et al.* [41] to be:

$$\kappa = -(\nabla \cdot \hat{n}) \quad (7)$$

In Eq.(7), \hat{n} is the unit normal vector. The normal is obtained based on the volume fraction gradient given by:

$$\hat{n} = \frac{\nabla \alpha_s}{|\nabla \alpha_s|} \quad (8)$$

The interface shape at the triple line, where the two phases meet the wall, is imposed by specifying \hat{n} through the specification of the contact angle as:

$$\hat{n} = \hat{n}_w \cos(\theta_w) + \hat{t}_w \sin(\theta_w) \quad (9)$$

where \hat{n}_w and \hat{t}_w are the unit vectors normal and tangential to the wall directed into the secondary fluid and wall.

2.2. Contact Angle Models

The VOF-CSF model requires contact angles to be specified as a boundary condition, and therefore an accurate specification of azimuthal contact angle variation is necessary. ElSherbini and Jacobi [17] summarized the contact angle functions predicted by earlier researchers (as shown in Figure 2). The contact angle variation predictions vary over a wide range but the important information is in the functional form of the variation. To obtain the functional form of the contact angle models included in Figure 2, the contact angle is normalized as follows:

$$\theta_{norm}(\phi) = \frac{\theta(\phi) - \theta_{rec}}{\theta_{adv} - \theta_{rec}} \quad (10)$$

Figure 3 shows the normalized contact angle variation. All the contact angle variations, except that in [24] which features a step function with a linear change, show a third-order polynomial variation. The third-order fit by El Sherbini and Jacobi [17] is a widely used, experimentally verified functional form for the contact angle, and is used in this study as well. The fit is given by:

$$\theta(\phi) = 2 \frac{\theta_{max} - \theta_{min}}{\pi^3} \phi^3 - 3 \frac{\theta_{max} - \theta_{min}}{\pi^2} \phi^2 + \theta_{max} \quad (11)$$

The inputs to the fit are the maximum and minimum contact angles, at the particular angle of inclination.

2.3. Solution Methodology

A square grid is used for the droplet simulations in FLUENT. A hemispherical cap of the required droplet size and material is initialized in the domain. The initial droplet domain and the boundary conditions applied are shown in Figure 4, along with the mesh in the background. Acceleration due to gravity is applied throughout the domain and is based on the angle of inclination of the surface being simulated. A no-slip boundary condition is specified at the bottom wall, while the remaining domain boundaries are specified-pressure boundaries set at a gauge pressure of zero. Utilizing droplet symmetry about the x-y plane ($z = 0$), only half of the domain is modeled and the results mirrored for presentation. On boundaries at which flow enters the calculation domain, the specified pressure is treated as the stagnation pressure; at outflow boundaries, the specified pressure is assumed to be the static pressure [39].

The third-order polynomial contact angle model discussed above (Eq.(11)) is implemented as a contact angle boundary condition on the contact line in the VOF-CSF model through user-defined functions (UDFs) in FLUENT. The inputs to the contact angle function, which are the maximum and minimum contact angles, are the experimentally measured advancing and receding angles at the particular angle of inclination (as discussed in Section 3).

2.4. Droplet Simulations

Two types of simulations are performed: (i) computation of the *inclination angle* corresponding to a *sessile* droplet on the incline, and (ii) computation of the *critical angle of inclination* corresponding to *critically sliding* droplets. We explain each in turn below.

All computations in this work are performed by specifying *a priori* the contact angle variation along the contact line. For sessile droplets, this variation is obtained from experiments by placing a droplet on an incline whose slope is too small to allow sliding, and measuring the advancing and receding contact angles for that inclination. Further details regarding the experimental procedure are provided in Section 3.3.2. Each inclination angle corresponds to a unique pair of advancing and receding contact angles. In the corresponding numerical simulation, we start by specifying the contact angles, and the corresponding gravity vector. If these values are self-consistent in the numerical simulation, the droplet will remain stationary. If they are not, the droplet will move up the incline if contact line forces overwhelm gravity, or down the incline if the reverse is true. The inclination angle β is varied in 1° increments until the droplet is rendered immobile. This is the *static angle of inclination*, β_{static} , for the unique pair of advancing and receding contact angles.

A similar procedure is adopted to determine the *critical angle of inclination*, *i.e.*, the angle of inclination for which the droplet just begins to slide down the incline. In this case, the contact angles specified in the simulation are taken from experiments at the critical inclination, *i.e.*, the inclination at which the droplet just begins to slide in the experiment. In the simulation, the droplet leading and trailing edge locations on the incline are monitored. The droplet is considered to be in sliding mode when the edge locations are moving down the incline. If the droplet is seen to be stationary at a given inclination, the angle of inclination is incremented by 1° by changing the components of the acceleration due to gravity appropriately. The process is continued until the droplet slides

down the incline. The corresponding angle of inclination is the numerically predicted *critical angle of inclination*, β_{crit} . Recently, a similar methodology was employed using Smoothed Particle Hydrodynamics by Das and Das [42] to model droplet critical angle of inclination. The contact angle along the contact line is computed using the modified Young equation.

3. EXPERIMENTAL SETUP AND PROCEDURES

To validate the numerical code, experimental measurements of the droplet profile and the advancing and receding contact angles were obtained as functions of droplet size and surface inclination.

To produce the desired test surfaces, indium-titanium oxide (ITO) slides were coated with a hydrophobic Teflon layer of approximately 50 nm thickness. This was achieved by spinning a 0.1% solution of Teflon-AF 1600 (DuPont, Wilmington, DE) in FC-77 [43] (3M, St. Paul, MN) at 1500 RPM for 30 s, followed by a hard baking process on a hot plate at 95°C for 45 min. The fabrication was conducted in the Birck Nanotechnology Center at Purdue University.

A goniometer system (CAM 101, KSV Instruments) was employed to image the contact angles and droplet sliding. The goniometer consists of a movable tilt stage for mounting the test surfaces, along with a CCD camera for imaging from one side. Contact angles can be measured to an accuracy of 0.1° using the image processing software provided with the system. The images are post-processed using MATLAB [44] to obtain the droplet profiles.

Two working fluids were employed: de-ionized water and ethylene glycol. De-ionized water was used for the sessile droplet tests. The working fluid was switched to ethylene glycol for the critical sliding experiments since evaporation of the de-ionized water changes the droplet volume during the experiment. Ethylene glycol, in contrast, does not evaporate at an appreciable rate. The experiment was initiated by dispensing a known volume of liquid on the Teflon-coated glass slide. With the help of a manual tilting stage, the surface was tilted until the required angle was reached. Tilting speeds for the sessile droplet tests with water were kept high (5°/min) so that evaporation is minimized; for the critical-angle determination with ethylene glycol, the surface tilt is changed more slowly (1°/min) so as to prevent the inadvertent imparting of additional momentum to the fluid. The goniometer CCD camera was used to capture images of the droplet at the desired inclinations. The uncertainty in volume measurement corresponding to the pixel resolution of 8 μm is 24 μm^3 (24x10⁻⁶ μl).

4. RESULTS AND DISCUSSION

4.1. Experimental Observations

4.1.1. Sessile Droplets

Images of de-ionized water droplets of volume 6 μl , 8 μl and 10 μl were obtained at surface inclinations of 5°, 10° and 15° (Figure 5). The corresponding advancing and receding contact angles are shown graphically in Figure 6. As β increases, the advancing contact angle increases and the receding contact angle decreases in order to balance the increased gravitational force. This effectively increases contact angle hysteresis, *i.e.*, the difference between the advancing and receding contact angles, which is also plotted in Figure 6.

4.1.2. Critical Sliding Droplets

The critical inclination is determined experimentally by increasing the angle of inclination in small increments starting from the horizontal, with the help of a manual tilting stage. Repeatability of the results was confirmed and the uncertainty in the measured critical angle of inclination was less than 0.5°. The critical surface inclination (β_{crit}) for droplet sizes of 4 μl and 8 μl was 18.8° and 12.8°, respectively. The larger droplets slide off at a smaller angle of inclination.

4.1.3. Advancing and Receding Contact Angles

The contact angle models require the advancing and receding contact angles to be provided as inputs. Hence, the dependence of these contact angles on liquid/air surface tension, droplet size, surface inclination and surface/liquid interaction needs to be determined *a priori*. The static contact angle θ_0 , *i.e.*, the value for zero angle of inclination, describes the baseline surface/liquid interaction. The rest of the parameters mentioned above may be represented by the Bond number, which is the ratio of gravitational to surface tension forces and is given by:

$$Bo = \frac{\rho g D^2 \sin \beta}{\sigma} \quad (12)$$

where σ is the surface tension, D is the diameter of the droplet when the inclination is horizontal, g is acceleration due to gravity and β is the angle of inclination.

Previous studies [13,17] have proposed correlations for the receding contact angle as a function of the advancing contact angle and the Bond number. As the advancing angle varies widely as a function of surface inclination, the static contact angle would be a simpler independent variable upon which to base correlations. Hence, in this work, the receding and advancing contact angles are found as a function of static contact angle and Bond number. The dependence of advancing and receding contact angles on Bond number is shown using the normalized values (θ_{adv} / θ_0) and ($\theta_{rec} / \theta_{adv}$) (Figure 7). The receding contact angle is normalized with the advancing contact angle for consistency with the literature [13,17]. The plot includes experimental data from both the sessile droplet experiments and the critical contact angle measurements. The critical contact angle measurements are differentiated in the figure with filled symbols. Linear fits to the θ_{adv} / θ_0 and $\theta_{rec} / \theta_{adv}$ data are plotted in the same figure, and are given by:

$$\theta_{adv} / \theta_0 = 1 + 0.123Bo \quad (13)$$

$$\theta_{rec} / \theta_{adv} = 1 - 0.298Bo \quad (14)$$

The correlation coefficients (R^2 values) for the fits are 0.92 and 0.97, respectively. Given the static contact angle and the Bond number, the contact angles can be predicted from Eq. (13) and (14). These equations are also used to validate the numerical model; the model is then applied to predict the droplet shape, contact line shape and contact area.

4.2. Numerical Results and Comparison with Experiments

The numerical simulations are first verified by comparing two-dimensional sessile droplet computations against analytical results. Simulations of three-dimensional sessile and critical droplets are then validated against experiments.

4.2.1. 2D Droplet – Analytical Verification

In order to verify the numerical analysis, a two-dimensional droplet is first considered, as shown in Figure 8(a). A two-dimensional semicircular droplet of radius R rests on a horizontal surface. A horizontal body force acts on the droplet with an equivalent acceleration due to gravity of g_{static} pointing to the right. The droplet attains an equilibrium shape with contact angles on the left and right edges reaching θ_{rec} and θ_{adv} , respectively. The conditions for the computation are given in Table 1.

The analytical solution for a 2D sessile droplet under the influence of a body force is given by a balance of surface tension and body forces, as shown in the free-body diagram in Figure 8(a):

$$(\cos \theta_{rec} - \cos \theta_{adv}) = \pi Bo_{static} \quad (15)$$

where θ_{rec} and θ_{adv} are the receding and advancing contact angles, $Bo_{static} = \frac{\rho D^2 g}{8\sigma}$, σ is the surface tension, and D is the diameter of the initial semicircle. If the balance in Eq. (15) is not satisfied by the numerical simulation, the droplet will either move up or down the incline depending on whether the left hand side or the right hand side dominates.

Numerical results from the 2D droplet simulations are shown in Figure 8(b-c). The droplet is seen to move to the left when the gravitational acceleration is less than g (*i.e.*, $Bo < Bo_{static}$) and is seen to move to the right when it is greater than g ($Bo > Bo_{static}$), in agreement with the analytical solution.

4.2.2. 3D Droplet on Incline – Experimental Validation

The numerical model developed in this work is employed next to study 3D sessile droplets on an incline. The experimentally measured advancing and receding contact angles at a given inclination of the surface are used in the contact angle model (Eq. (11)). With the specified contact angles, the angle of inclination is varied in the numerical model and the angle of inclination at which the droplet is stable and stationary is predicted. The reported inclination angle is this numerical value. If the simulation result is consistent with the experiment, *i.e.*, the numerical force balance is accurate, the simulated droplet must remain stationary at the same angle of inclination as the experiment. The properties of water [39, 45] and ethylene glycol [39,46] used in the simulations are given in Table 2.

To understand the effect of droplet volume on the angle of inclination, results for different droplet volumes are compared at a fixed angle of inclination ($\beta = 10^\circ$) in Figure 9. The inputs to the numerical model are the experimentally measured static advancing and receding contact angles for different droplet volumes which are also listed on the x-axis. The uncertainty, defined by the step change in the angle of inclination between

simulations, is 1° and is shown as error bars in the figure. Also shown is the experimental uncertainty. The numerical predictions are all within an error band of 1° of the experimental inclination value of $\beta = 10^\circ$.

A comparison between experiments and numerical simulations for fixed droplet volume at various inclinations is shown in Figure 10. As the angle of inclination is increased in the experiments, the advancing angle increases and the receding angle decreases. Again, the comparison between the experiments and simulations is within the error bar of 1° in the simulated inclination angle.

Another important comparison for validation is the predicted and measured droplet shape of the sessile droplet. Figure 11 shows the droplet shape for a $10\ \mu\text{l}$ water droplet at a 10° inclination. The color contour shows the predicted droplet shape whereas the dark outline shows the measured shape. The shape of the predicted droplet is defined as that of the $\alpha = 0.5$ volume fraction surface. The experimental droplet shape was obtained by post-processing the data with MATLAB [44] using the Canny edge detection method [47]. The comparisons show excellent agreement between the numerical predictions and experimental measurements.

4.3. Critical Angle of Inclination

The numerical model is now used to predict the critical angle of inclination. Again, the inputs are the advancing and receding contact angles at the critical inclination from experiment. Figure 12 shows a comparison of the numerical predictions with experimental measurements of the critical angle of inclination. The numerical predictions and experimental measurements are in good agreement, with the numerical predictions matching the experiments to within the numerical error bar of 1° .

4.4. Droplet Contact Line Shape and Contact Area

The predicted contact line shapes for sessile water droplets of different droplet volumes at $\beta = 10^\circ$ are shown in Figure 13. The contact line based on a spherical-cap assumption is also shown in the figure with dashed lines. The shape of the spherical cap is obtained by matching the experimental droplet volume to the region of a sphere above a plane and experiencing a contact angle with the plane equal to the static contact angle. The variation with inclination was found to be negligible and hence is not shown separately. This is due to the low Bond numbers, which imply that the droplet shape is governed by surface tension forces rather than body forces. From the figure, it is evident that the droplet contact area is almost circular, which agrees with the low Bond number argument. The associated contact areas and lengths of the droplets for various droplet volumes are given in Table 3. The contact length/diameter and contact area of the corresponding spherical cap are also shown in the table in parentheses. The contact length/diameter ($D_{contact}$) and contact area ($A_{contact}$) based on the spherical-cap assumption are given by:

$$D_{contact} = \left(\frac{24V \sin^3 \theta_0}{\pi (2 - 3 \cos \theta_0 + \cos^3 \theta_0)} \right)^{1/3} \quad (16)$$

$$A_{contact} = \frac{\pi D_{contact}^2}{4} \quad (17)$$

The spherical-cap assumption underpredicts the droplet length and contact area by 7.7% and 3.5%, respectively, compared to the numerical predictions. This is due to the stretching of the droplet in the predictions due to the body forces acting along the incline, which is not accounted for in the spherical-cap model.

5. CONCLUSIONS

A numerical model for predicting static droplet shapes and critical droplet motion on an inclined plane has been developed. A contact angle model that is a function of the azimuthal angle is implemented in the VOF-CSF model. The model is verified against analytical solutions for two-dimensional cases. The numerical model is successful in simulating the behavior of sessile droplets on an incline. Results from the model are compared with experimental measurements of droplet shape and angle of inclination and show good agreement. Correlations are developed for the advancing and receding angles as functions of Bond number and the initial static contact angle. The droplet shape, contact line profile and the contact area are predicted. For the experimental droplet sizes and angles of inclination tested, a spherical-cap assumption is shown to capture the trend of the contact area and droplet length well. However, the spherical-cap assumption underpredicts the droplet length and area as it does not account for the elongation of the droplet due to the body forces. The model is also used to predict critical sliding of droplets and again shows good agreement with experiment. Further additions to the model are in progress to predict droplets under electrowetting actuation forces.

ACKNOWLEDGEMENTS

The authors acknowledge financial support for this work through the Cooling Technologies Research Center, an NSF Industry/University Cooperative Research Center at Purdue University.

REFERENCES

- [1] T. Wang, J. L. Gaddis, X. Li, Mist/steam heat transfer of multiple rows of impinging jets, *International Journal of Heat and Mass Transfer*, 48 (2005) 5179-5191.
- [2] N. Kumari, V. Bahadur, M. Hodes, T. Salamon, P. Kolodner, A. Lyons, S.V., Garimella, Analysis of evaporating mist flow for enhanced convective heat transfer, *International Journal of Heat and Mass Transfer* 53 (2010) 3346-3356.
- [3] T.A. Shedd, A.G. Pautsch, Spray impingement cooling with single-and multiple-nozzle arrays. Part II: Visualization and empirical models, *International Journal of Heat and Mass Transfer* 48 (2005) 3176-3184.
- [4] S. Freund, A.G. Pautsch, T.A. Shedd, S. Kabelac, Local heat transfer coefficients in spray cooling systems measured with temperature oscillation IR thermography, *International Journal of Heat and Mass Transfer* 50 (2007) 1953-1962.
- [5] C. Graham, P. Griffith, Drop size distributions and heat transfer in dropwise condensation, *International Journal of Heat and Mass Transfer* 16 (1973) 337-346.
- [6] V. Bahadur, S.V. Garimella, An energy-based model for electrowetting-induced droplet actuation, *Journal of Micromechanics and Microengineering*, 16 (2006) 1494-1503.
- [7] N. Kumari, V. Bahadur, S.V. Garimella, Electrical actuation of dielectric droplets, *Journal of Micromechanics and Microengineering*, 18 (2008) 085018.

- [8] V. Bahadur, S.V. Garimella, Energy minimization-based analysis of electrowetting for microelectronics cooling applications, *Microelectronics Journal*, 39 (2008) 957-965.
- [9] S.R. Annapragada, J.Y.. Murthy, S.V. Garimella, Prediction of droplet dynamics on an incline, *International Journal of Heat and Mass Transfer*, (2010), in review.
- [10] B. Berge, J. Peseux, Variable focal lens controlled by an external voltage: an application of electrowetting, *The European Physical Journal E: Soft Matter and Biological Physics* 3 (2000) 159-163.
- [11] G. Macdougall, C. Ockrent, Surface energy relations in liquid/solid systems. I. The adhesion of liquids to solids and a new method of determining the surface tension of liquids, *Proceedings Royal Society London, Ser. A*, 180 (1942) 151-173.
- [12] Y.I. Frenkel, On the behavior of liquid drops on a solid surface 1. The sliding of drops on an inclined surface, *Journal of Experimental and Theoretical Physics U.S.S.R.*, 18, (1948) 659; <http://lanl.arxiv.org/abs/physics/0503/0503051.pdf>.
- [13] C.W. Extrand, A.N. Gent, Retention of liquid drops by solid surfaces, *Journal Colloid Interface Science*, 138 (1990) 431-442.
- [14] C.W. Extrand, Y.Kumagai, Liquid drops on an inclined plane: the relation between contact angles, drop shape, and retentive force, *Journal Colloid Interface Science*, 170 (1995) 515-521.
- [15] E.B. Dussan, R.T.-P. Chow, On the ability of drops or bubbles to stick to non-horizontal surfaces of solids, *Journal Fluid Mechanics*, 137 (1983) 1-29.
- [16] E. Wolfram, R. Faust, in: J. F. Padday (Ed.), *Wetting, Spreading, and Adhesion*, Academic Press, New York, 1978, 213–222.
- [17] A.I. ElSherbini, A.M. Jacobi, Liquid drops on vertical and inclined surfaces: I. An experimental study of drop geometry, *Journal Colloid Interface Science*, 273 (2004) 556-565.
- [18] A.I. ElSherbini, A.M. Jacobi, Liquid drops on vertical and inclined surfaces: II. A method for approximating drop shapes, *Journal Colloid Interface Science*, 273 (2004) 566-575.
- [19] A.I. ElSherbini, A.M. Jacobi, Retention forces and contact angles for critical liquid drops on non-horizontal surfaces, *Journal Colloid Interface Science*, 299 (2006) 841-849.
- [20] A.I. ElSherbini, A.M. Jacobi, A model for condensate retention on plain-fin heat exchangers, *Journal Heat Transfer*, 128 (2006) 427-433.
- [21] H. Merte, C. Yamali, Profile and departure size of condensation drops on vertical surfaces, *Warme Stoffubertrag*, 17 (1983) 171-180.
- [22] H. Merte, S. Son, Further considerations of two-dimensional condensation drop profiles and departure sizes, *Warme Stoffubertrag*, 21 (1987) 163-168.
- [23] F. Milinazzo, M. Shinbrot, A numerical study of a drop on a vertical wall, *Journal Colloid Interface Science*, 121 (1988) 254-264.
- [24] P. Dimitrakopoulos, J.J.L. Higdon, On the gravitational displacement of three-dimensional fluid droplets from inclined solid surfaces, *Journal of Fluid Mechanics*, 395 (1999) 181-209.
- [25] S.D. Iliev, Static drops on an inclined plane: Equilibrium modeling and numerical analysis, *Journal Colloid Interface Science*, 194 (1997) 287-300.
- [26] S.S. Manna, H.J. Herrmann, D.P. Landau, A stochastic method to determine the shape of a drop on a wall, *Journal Statistical Physics*, 66 (1992) 1155-1163.
- [27] R.A. Brown, F.M. Orr Jr., L.E. Scriven, Static drop on an inclined plate: Analysis by the finite element method, *Journal Colloid Interface Science*, 73 (1980) 76-87.
- [28] S.F. Lunkad, V.V. Buwa, K.D.P. Nigam, Numerical simulations of drop impact and spreading on horizontal and inclined surfaces, *Chemical Engineering Science*, 62 (2007) 7214-7224.

- [29] Š. Šikalo, H.-D. Wilhelm, I. V. Roisman, S. Jakirlić, C. Tropea, Dynamic contact angle of spreading droplets: Experiments and simulations, *Physics of Fluids*, 17 (2005) 062103.
- [30] S. Zhen-Hai, H. Rui-Jing, Simulation solution for micro droplet impingement on a flat dry surface, *Chinese Physics B*, 17 (2008) 3185-3188.
- [31] A. Sanjeev, Computational study of surfactant-induced modification of droplet impact dynamics and heat transfer on hydrophobic and hydrophilic surfaces, M.S. Thesis University of Cincinnati, 2008.
- [32] H. Huang, P. Meakin, M. Liu, Computer simulation of two-phase immiscible fluid motion in unsaturated complex fractures using a volume of fluid method, *Water Resources Research*, 41 (2005) W12413.
- [33] S. van Mourik, A.E.P. Veldman, M.E. Dreyer, Simulation of capillary flow with a dynamic contact angle, *Microgravity Science Technology*, XVII-3 (2005) 87-93.
- [34] L. Chen, S.V. Garimella, J.A. Reizes, E. Leonardi, The development of a bubble rising in a viscous liquid, *Journal Fluid Mechanics*, 387 (1999) 61-96.
- [35] L. Chen, S.V. Garimella, J.A. Reizes, E. Leonardi, Motion of interacting gas bubbles in a viscous liquid including wall effects and evaporation, *Numerical Heat Transfer, Part A: Applications*, 31 (1997) 629-654.
- [36] S. Afkhami, Ph.D. Thesis, University of Toronto, 2008.
- [37] T. D. Blake, *Wettability* J.C. Berg, (Ed.), (1993) Marcel Dekker, New York 251.
- [38] J.E. Seebergh, J. C. Berg, Dynamic wetting in the low capillary number regime, *Chemical Engineering Science*, 47 (1992) 4455-4464.
- [39] *Fluent 6.3 Users Guide*, Ansys Inc. Lebanon, NH, 1996.
- [40] D.L. Youngs, 1982, *Numerical Methods for Fluid Dynamics*, Academic Press, New York.
- [41] J.U. Brackbill, D.B. Kothe, C. Zemach, A continuum method for modeling surface tension, *Journal Computational Physics*, 100 (1992) 335-354.
- [42] A.K. Das, P.K. Das, Simulation of Drop Movement over an Inclined Surface Using Smoothed Particle Hydrodynamics, *Langmuir*, 25 (2009) 11459–11466.
- [43] FC 77 product manual, 3M, St. Paul, MN, 2006.
- [44] *MATLAB: The language of technical computing*, version 6.5, The MathWorks, Inc. Natick, MA, 2002.
- [45] F. Felix, *Water, A Matrix of Life*, 2nd Ed. The Royal Society of Chemistry 2000.
- [46] H.P. Schreiber, F. Ewane-Ebele, On the surface tension and its temperature variation in film-forming polymers, *The Journal of Adhesion*, 9 (1978) 175-184.
- [47] J. Canny, A Computational Approach to Edge Detection, *IEEE Transactions on Pattern Analysis and Machine Intelligence* 8 (1986) 679-698.

FIGURE CAPTIONS

- Figure 1. Schematic diagram of sessile droplet and associated terminology.
- figure 2. Azimuthal contact angle variation predictions (with parameters from [17]).
- figure 3. Normalized azimuthal contact angle variation predictions along the droplet using different models in the literature.
- figure 4. Initial droplet domain along with boundary conditions. The mesh is shown in the background.
- figure 5. Water droplet images at inclinations of 5, 10 and 15 deg for droplet sizes of (a) 6 μl , (b) 8 μl , and (c) 10 μl .
- figure 6. (a) advancing contact angle, (b) receding contact angle, and (c) contact angle hysteresis for various droplet sizes and surface inclinations with sessile water droplets.
- figure 7. Normalized contact angles as a function of bond number, bo . The data are fit by straight lines with a y-intercept of unity. The contact angles at the critical angle of inclination are indicated by filled symbols.
- figure 8. (a) free body diagram of the 2d droplet, (b) numerical simulation at $bo = 0.10$ ($bo_{\text{static}} = 0.11$) and at time = 0.1 s, and (c) numerical simulation at $bo = 0.12$ ($bo_{\text{static}} = 0.11$) and at time = 0.1 s. The red region is the droplet, and the blue region is air. The initial droplet location is shown as a white outline.
- figure 9. Comparison between numerical and experimental results for static inclination angle as a function of droplet volume at $\beta = 10^\circ$ for water.
- figure 10. Comparison between numerical and experimental results for static inclination angle as a function of angle of inclination for a water droplet volume of 8 μl .
- figure 11. Comparison of computed and measured sessile water droplet shapes. Numerical simulation (contours), experimental measurement (black line). Droplet volume is 10 μl and angle of inclination (β) is 10° .
- figure 12. Comparison of numerical predictions and experimental measurements of critical inclination angle for ethylene glycol droplets.
- figure 13. Droplet contact line predictions for sessile water droplets of various sizes. The results from the spherical cap assumption are shown as dashed lines.

Table 1. Analytical model parameters for 2D droplet.

Parameter	Value
Static Bond number, Bo_{static}	0.11
Receding contact angle, θ_{rec}	90°
Advancing contact angle, θ_{adv}	110°

Table 2. Properties of water and ethylene glycol.

<i>Property</i>	<i>Water</i>	<i>Ethylene Glycol</i>
Density, ρ , kg/m ³	998.2	1111.4
Surface tension, σ , N/m	0.072	0.047
Viscosity, μ , N s/m ²	0.001003	0.0161

Table 3. Droplet length and contact area predictions for different droplet volumes. Values obtained using the spherical-cap assumption are given in parentheses.

<i>Droplet volume (μl)</i>	<i>6</i>	<i>8</i>	<i>10</i>
Droplet length (mm)	2.21 (2.04)	2.43 (2.24)	2.62 (2.42)
Contact area (mm^2)	3.35 (3.26)	4.16 (3.95)	4.68 (4.59)

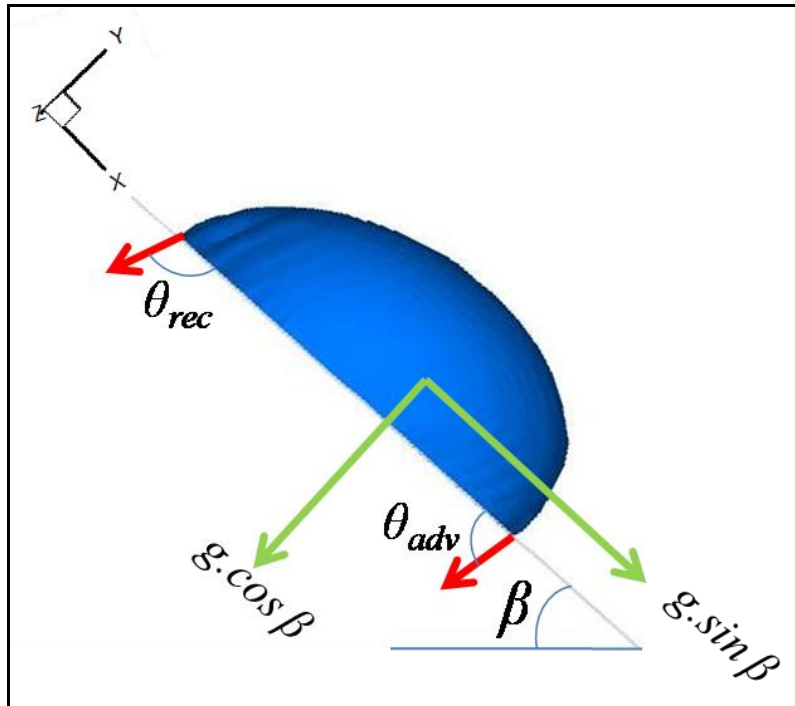


Figure 1. Schematic diagram of sessile droplet and associated terminology.

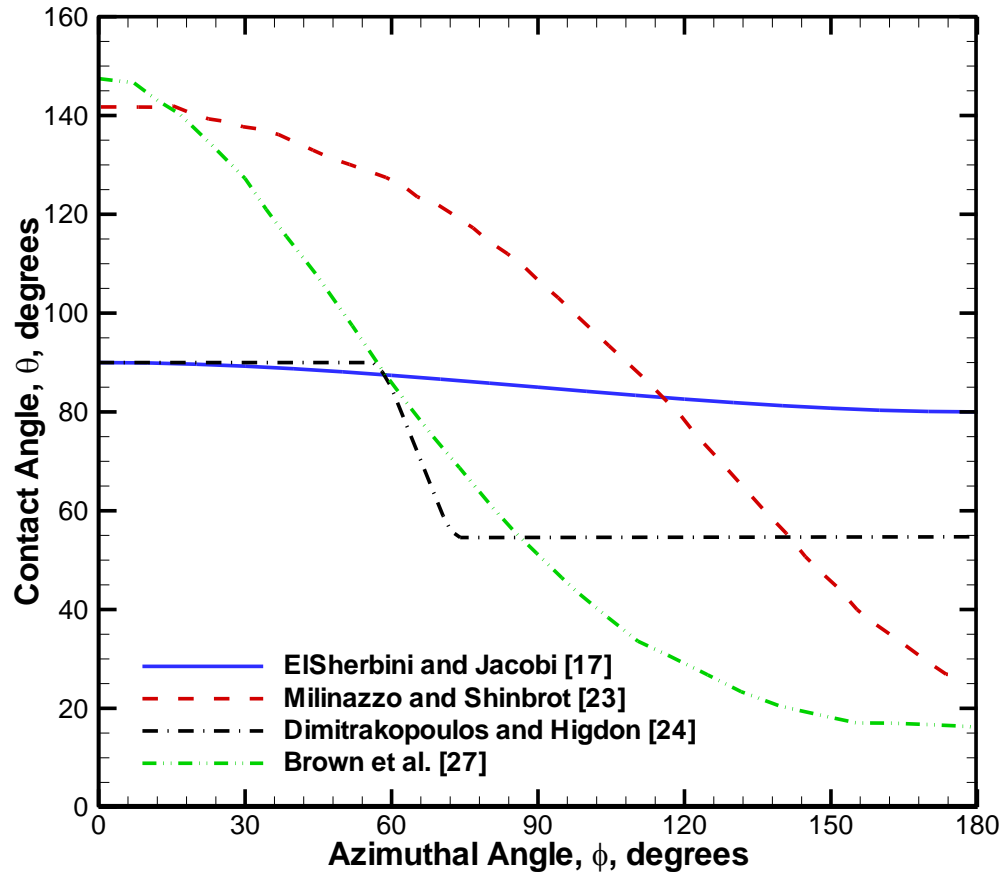


Figure 2. Azimuthal contact angle variation predictions (with parameters from [17]).

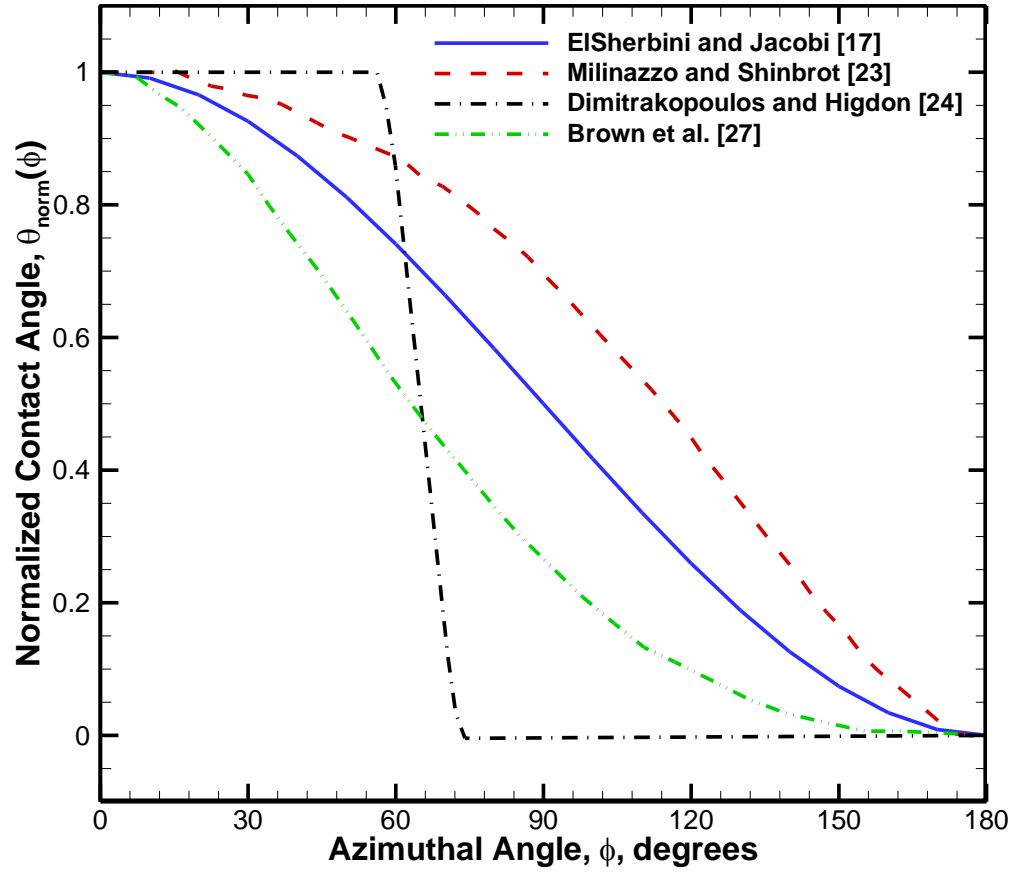


Figure 3. Normalized azimuthal contact angle variation predictions along the droplet using different models in the literature.

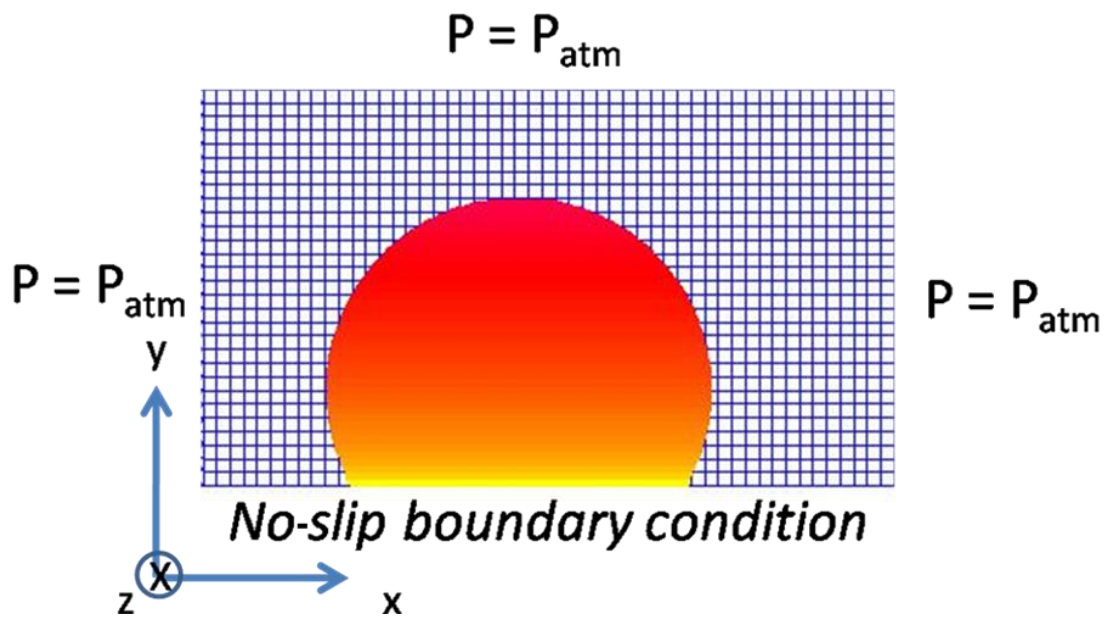
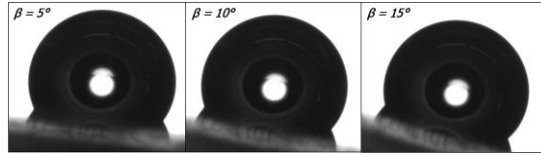
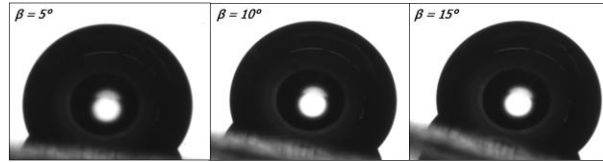


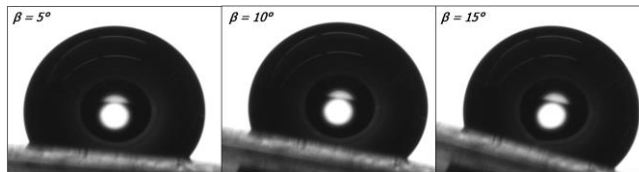
Figure 4. Initial droplet domain along with boundary conditions. The mesh is shown in the background.



(a)



(b)



(c)

Figure 5. Water droplet images at inclinations of 5, 10 and 15 deg for droplet sizes of (a) 6 μl , (b) 8 μl , and (c) 10 μl .

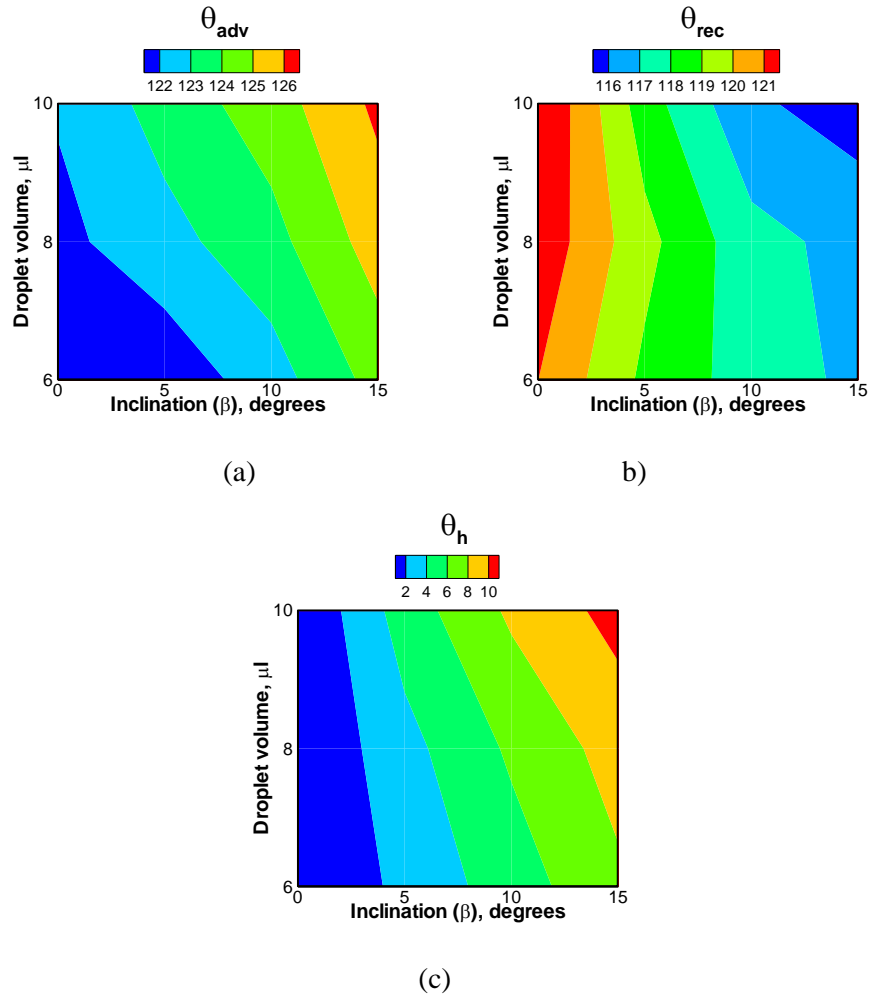


Figure 6. (a) Advancing contact angle, (b) receding contact angle, and (c) contact angle hysteresis for various droplet sizes and surface inclinations with sessile water droplets.

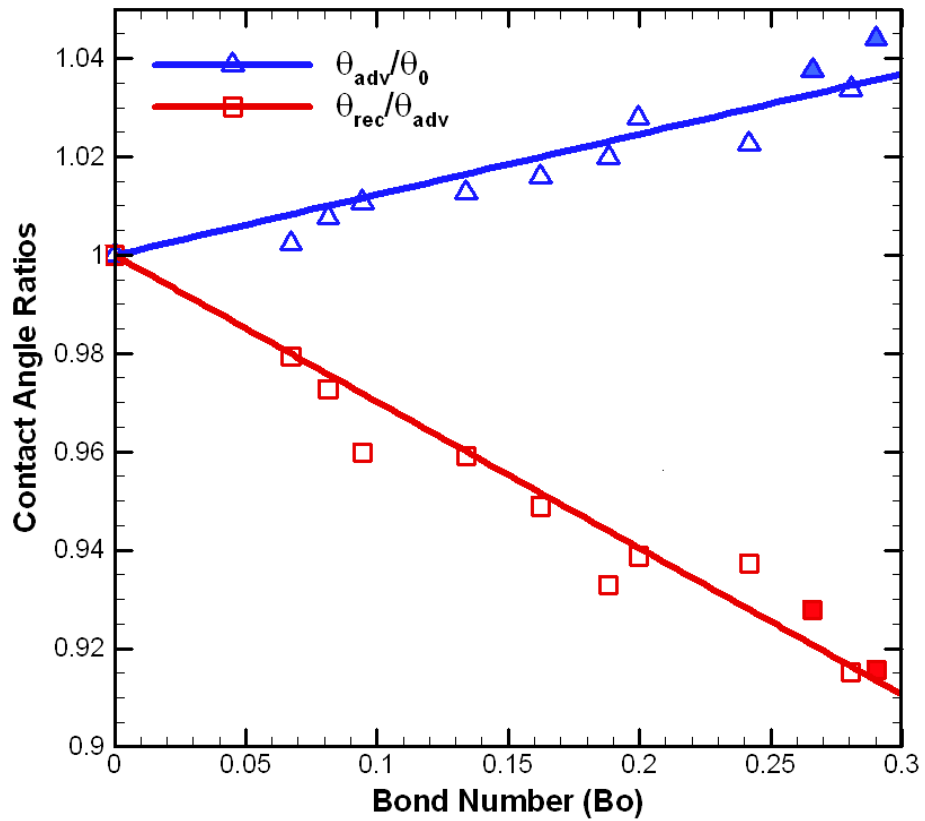


Figure 7. Normalized contact angles as a function of Bond number, Bo. The data are fit by straight lines with a y-intercept of unity. The contact angles at the critical angle of inclination are indicated by filled symbols.

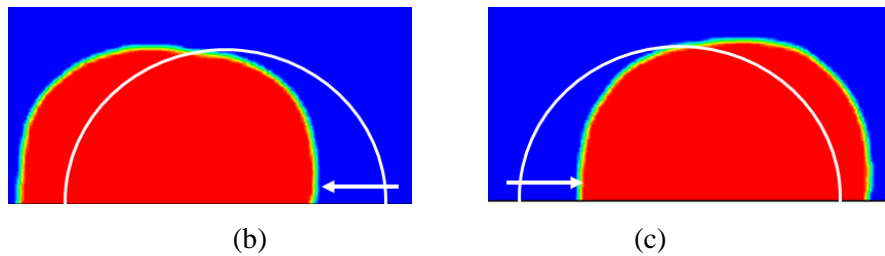
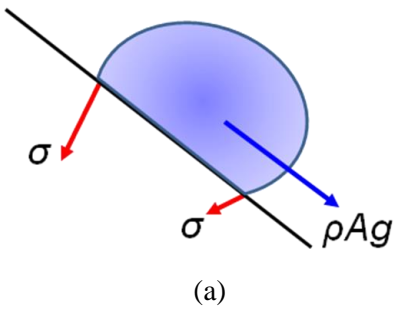


Figure 8. (a) Free body diagram of the 2D droplet, (b) numerical simulation at $Bo = 0.10$ ($Bo_{static} = 0.11$) and at time = 0.1 s, and (c) numerical simulation at $Bo = 0.12$ ($Bo_{static} = 0.11$) and at time = 0.1 s. The red region is the droplet, and the blue region is air. The initial droplet location is shown as a white outline.

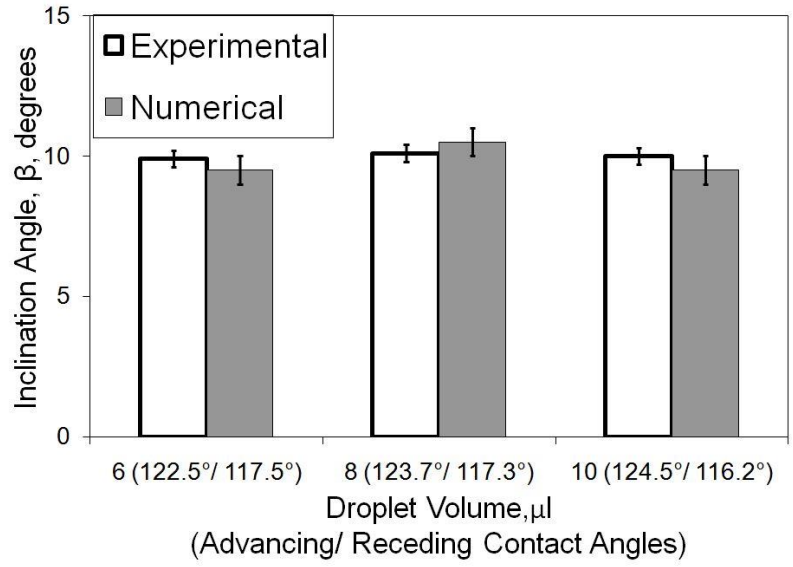


Figure 9. Comparison between numerical and experimental results for static inclination angle as a function of droplet volume at $\beta = 10^\circ$ for water.

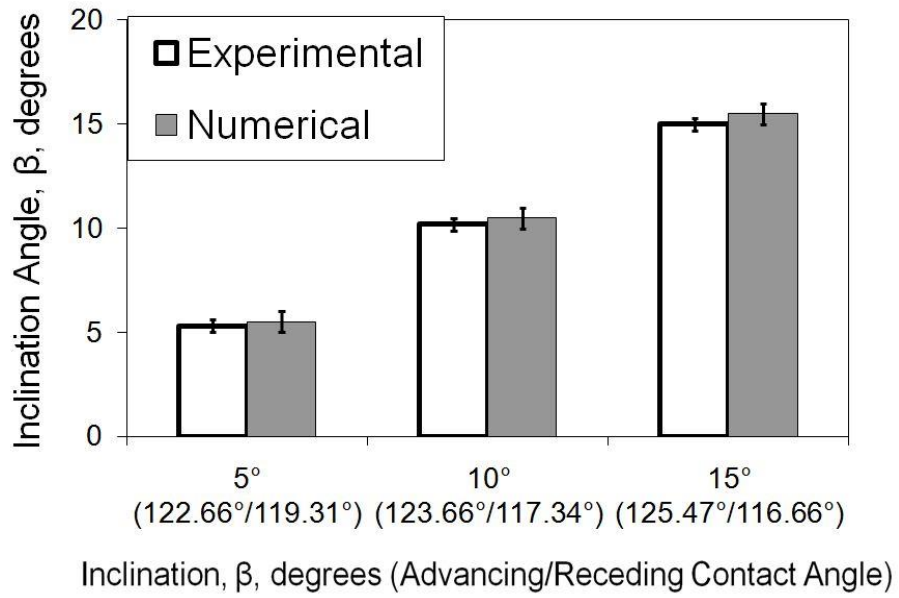


Figure 10. Comparison between numerical and experimental results for static inclination angle as a function of angle of inclination for a water droplet volume of 8 μl .

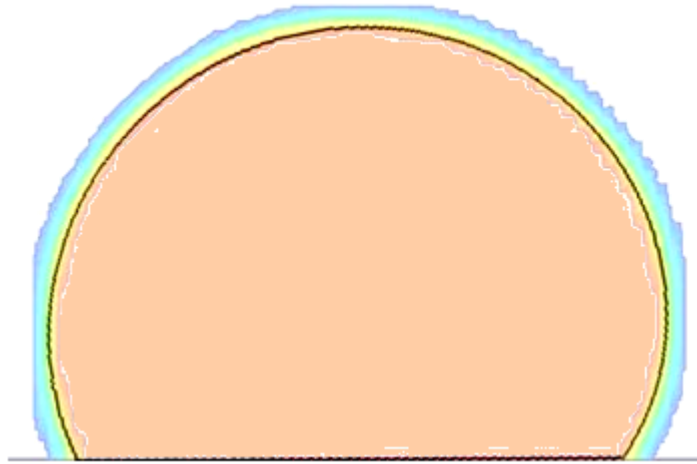


Figure 11. Comparison of computed and measured sessile water droplet shapes. Numerical simulation (contours), experimental measurement (black line). Droplet volume is $10 \mu\text{l}$ and angle of inclination (β) is 10° .

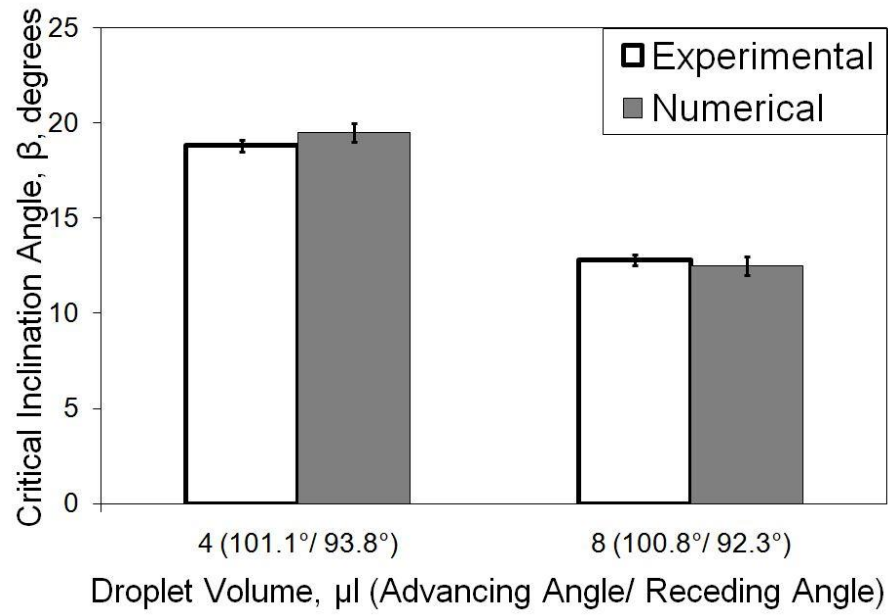


Figure 12. Comparison of numerical predictions and experimental measurements of critical inclination angle for ethylene glycol droplets.

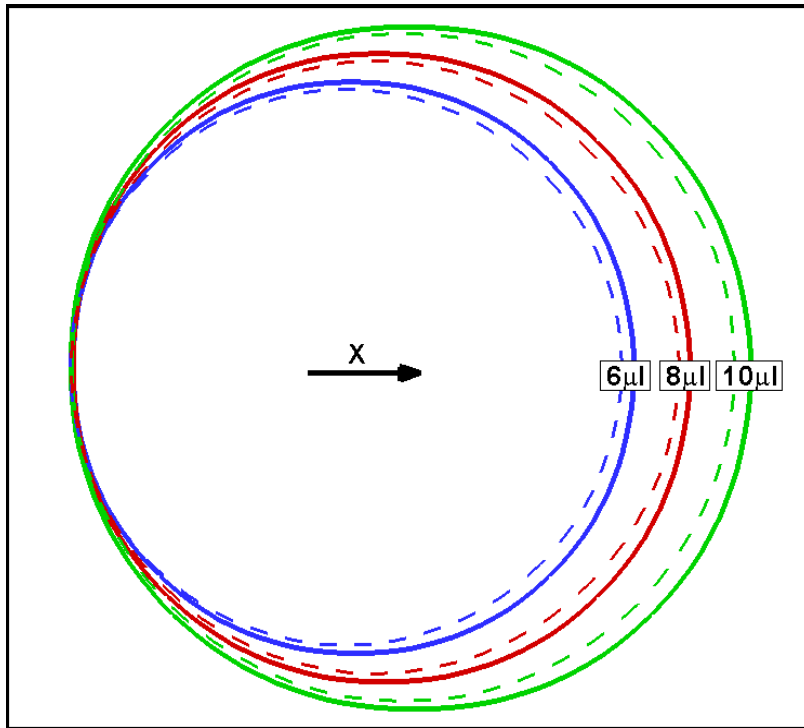


Figure 13. Droplet contact line predictions for sessile water droplets of various sizes. The results from the spherical cap assumption are shown as dashed lines.